REPORT DOCUMENTATION PAGE

Form Approved OMB No. 0704-0188

1a. REPORT SECURITY CLASSIFICATION: Unclassified

1b. RESTRICTIVE MARKINGS:

2a. SECURITY CLASSIFICATION AUTHORITY:

3. DISTRIBUTION/AVAILABILITY OF REPORT: Approved for public release; Distribution unlimited

2b. DECLASSIFICATION/DOWNGRADING SCHEDULE:

4. PERFORMING ORGANIZATION REPORT NUMBER(S): PL-TR-91-2111

5. MONITORING ORGANIZATION REPORT NUMBER(S):

6a. NAME OF PERFORMING ORGANIZATION: Phillips Laboratory

6b. OFFICE SYMBOL (If applicable): PHP

7a. NAME OF MONITORING ORGANIZATION:

6c. ADDRESS (City, State, and ZIP Code): Hanscom AFB, Massachusetts 01731-5000

7b. ADDRESS (City, State, and ZIP Code):

8a. NAME OF FUNDING/SPONSORING ORGANIZATION:

8b. OFFICE SYMBOL (If applicable):

9. PROCUREMENT INSTRUMENT IDENTIFICATION NUMBER:

8c. ADDRESS (City, State, and ZIP Code):

10. SOURCE OF FUNDING NUMBERS

PROGRAM ELEMENT NO.	PROJECT NO	TASK NO	WORK UNIT ACCESSION NO.
62101F	7601	22	03

11. TITLE (Include Security Classification): A Statistical Study on the Effects of IMF B z and Solar Wind Speed on Auroral Ion and Electron Precipitation

12. PERSONAL AUTHOR(S): D.H. Brautigam, M.S. Gussenhoven, D.A. Hardy

13a. TYPE OF REPORT	13b. TIME COVERED	14. DATE OF REPORT (Year, Month, Day)	15. PAGE COUNT
Reprint	FROM _____ TO _____	1991 May 10	14

16. SUPPLEMENTARY NOTATION: Reprinted from Journal of Geophysical Research, Vol. 96, No. A4, Pages 5525-5538, April 1, 1991

17. COSATI CODES		
FIELD	GROUP	SUB-GROUP

18. SUBJECT TERMS (Continue on reverse if necessary and identify by block number): Wind speed, Ion electron

19. ABSTRACT (Continue on reverse if necessary and identify by block number)

The variation in the average particle number and energy flux in the high-latitude region is determined as a function of the solar wind velocity, V_{sw}, and the z component of the interplanetary magnetic field, B_z. The study is made using the data from the SSJ/4 detectors on the satellites of the Defense Meteorological Satellite Program. In the study the high-latitude region is divided into spatial elements in magnetic local time and corrected geomagnetic latitude. One such matrix of spatial divisions is constructed for each of 30 paired ranges of values in V_{sw} and B_z. There are six divisions in B_z covering the range from −10 to +10 nT and five divisions in velocity covering the range from 200 to 800 km/s. Using approximately 34 million SSJ/4 spectra, the average electron and ion spectra are determined in each spatial element for each of the 30 paired values of V_{sw} and B_z. From the average spectra, the average integral energy and number fluxes for electrons and ions are calculated in each spatial bin. These values are then spatially integrated to give the average hemispheric inputs of the integral particle energy and number flux. Both quantities are found to vary in a simple and consistent manner with both V_{sw} and B_z. For both electrons and ions the variation with B_z tends to a minimum value for weak to moderately strong B_z positive. For decreasing values of B_z from the minimum, both quantities increase at a rate greater than linear. For increasing values of B_z from the minimum, both quantities tend to increase, least for the hemispheric electron energy flux and most for the hemispheric ion

(Cont'd)

20. DISTRIBUTION/AVAILABILITY OF ABSTRACT: ☐ UNCLASSIFIED/UNLIMITED ☒ SAME AS RPT. ☐ DTIC USERS

21. ABSTRACT SECURITY CLASSIFICATION: Unclassified

22a. NAME OF RESPONSIBLE INDIVIDUAL: M.S. Gussenhoven

22b. TELEPHONE (Include Area Code): (617) 377-3213

22c. OFFICE SYMBOL: PHP

DD Form 1473, JUN 86 — Previous editions are obsolete. — SECURITY CLASSIFICATION OF THIS PAGE: Unclassified

Cont of Block 19:

number flux. The variation in both quantities with V_{sw} for both electrons and ions is generally linear with the steepest slopes for the electron hemispheric energy flux. The variation with B_z and V_{sw} for all four quantities can be well fit by a simple quadratic equation either of the form $f(B_z, V_{sw}) = a(B_z - b)^2 + cV_{sw} + d$ or $f(B_z, V_{sw}) = [a(B_z - b)^2 + 1][cV_{sw} + d]$. Either form indicates that the variation is no greater than quadratic in B_z and no more than linear in V_{sw} and that the variation is approximately symmetric for values above and below the minimum value of B_z, namely, b. This result is significantly different than either the half-wave rectifier or epsilon function for describing the solar-wind magnetospheric interaction.

JOURNAL OF GEOPHYSICAL RESEARCH, VOL. 96, NO. A4, PAGES 5525–5538, APRIL 1, 1991

A Statistical Study on the Effects of IMF B_z and Solar Wind Speed on Auroral Ion and Electron Precipitation

D. H. BRAUTIGAM, M. S. GUSSENHOVEN, AND D. A. HARDY

Geophysics Laboratory, Hanscom Air Force Base, Massachusetts

The variation in the average particle number and energy flux in the high-latitude region is determined as a function of the solar wind velocity, V_{sw}, and the z component of the interplanetary magnetic field, B_z. The study is made using the data from the SSJ/4 detectors on the satellites of the Defense Meteorological Satellite Program. In the study the high-latitude region is divided into spatial elements in magnetic local time and corrected geomagnetic latitude. One such matrix of spatial divisions is constructed for each of 30 paired ranges of values in V_{sw} and B_z. There are six divisions in B_z covering the range from −10 to +10 nT and five divisions in velocity covering the range from 200 to 800 km/s. Using approximately 34 million SSJ/4 spectra, the average electron and ion spectra are determined in each spatial element for each of the 30 paired values of V_{sw} and B_z. From the average spectra, the average integral energy and number fluxes for electrons and ions are calculated in each spatial bin. These values are then spatially integrated to give the average hemispheric inputs of the integral particle energy and number flux. Both quantities are found to vary in a simple and consistent manner with both V_{sw} and B_z. For both electrons and ions the variation with B_z tends to a minimum value for weak to moderately strong B_z positive. For decreasing values of B_z from the minimum, both quantities increase at a rate greater than linear. For increasing values of B_z from the minimum, both quantities tend to increase, least for the hemispheric electron energy flux and most for the hemispheric ion number flux. The variation in both quantities with V_{sw} for both electrons and ions is generally linear with the steepest slopes for the electron hemispheric energy flux. The variation with B_z and V_{sw} for all four quantities can be well fit by a simple quadratic equation either of the form $f(B_z, V_{sw}) = a(B_z - b)^2 + cV_{sw} + d$ or $f(B_z, V_{sw}) = [a(B_z - b)^2 + 1][cV_{sw} + d]$. Either form indicates that the variation is no greater than quadratic in B_z and no more than linear in V_{sw} and that the variation is approximately symmetric for values above and below the minimum value of B_z, namely, b. This result is significantly different than either the half-wave rectifier or epsilon function for describing the solar–wind magnetospheric interaction.

1. INTRODUCTION

This study is designed to quantify the response of auroral precipitation to varying solar wind conditions. We parameterize auroral precipitation by the precipitating electron and ion hemispheric energy flux and number flux and the solar wind condition by the z component of the interplanetary magnetic field (IMF B_z) and the solar wind velocity (V_{sw}). We have previously quantified the response of auroral precipitation to varying geomagnetic activity using the Kp index. This work may be found in the papers by *Hardy et al.* [1985] (electron response) and *Hardy et al.* [1989] (ion response), which are referred to as paper 1 (electrons) and paper 2 (ions) throughout the remainder of this paper. Although sorting by Kp provides insight into the dependence of auroral fluxes and morphology on geomagnetic activity, it does not directly address the question of which external mechanisms are responsible for driving the magnetospheric processes. We therefore extend our work, replacing Kp with B_z and V_{sw} as ordering parameters.

It is widely acknowledged that the polarity and magnitude of IMF B_z play the major role in controlling the merging process between closed geomagnetic field lines and open interplanetary magnetic field lines [*Russell*, 1986; *Baumjohann and Haerendel*, 1985]. As such, it significantly affects the Earth's magnetic field topology and plays a fundamental role in modulating the strength of the solar wind–magnetosphere coupling. The solar wind speed also plays a significant role both electrodynamically, through the impressed electric field ($V_{sw}B_z$) [*Maezawa and Murayama*, 1986], and magnetohydrodynamically [*Spreiter and Alksne*, 1969].

Gussenhoven [1988] defined the ground state of the magnetosphere as the condition resulting from a period of extended minimal solar wind–magnetosphere coupling during which its energy content has decayed to a minimum. By examining low-altitude signatures of magnetospheric activity (relating to both auroral oval and polar cap phenomena) under variable solar wind conditions, she concludes that the baseline magnetosphere occurs after a period of low B_z north (near $B_z = 0$) and low V_{sw}. The polarity of B_z is critical in determining the manner in which the magnetosphere is energized. A southward B_z leads to an energetic oval and a quiet polar cap, whereas a northward B_z leads to a quiet oval and a more active polar region. Low-altitude signatures of magnetospheric processes driven by B_z south (active auroral oval) and by strong B_z north (active polar cap) are beginning to define the full range of processes by which the magnetosphere is energized. An accurate assessment of the dynamical state of the magnetosphere must involve consideration of activity in the polar cap as well as in the auroral oval.

The solar wind and IMF energize the magnetosphere through a number of interrelated processes which include impressing electric potentials, driving currents, and energizing particles. Despite the complexity of the coupling, high correlations have been obtained between ionospheric signatures of these processes and solar wind parameters. Low-altitude measures of magnetospheric activity that have been

Paper number 91JA00157.

correlated include (1) the cross–polar cap potential, (2) the auroral electrojet current indices *AE* (*AL*, *AU*), (3) the field-aligned current intensity, (4) the frequency and intensity of polar cap arcs, and (5) the precipitating particles (auroral boundaries and hemispheric fluxes).

Reiff and Luhmann [1986] have reviewed efforts to model the cross–polar cap voltage (V_{pc}) as a function of B_z and V_{sw}. They report that for B_z south, dayside merging is responsible for between 80 and 95% of V_{pc} with the remainder due to nightside magnetotail-lobe merging and magnetopause boundary layer quasi-viscous interaction. For B_z north, the contribution to V_{pc} from dayside merging is greatly diminished, while that from the latter two processes increases slightly, so that functions which best model V_{pc} are those that do not cut off sharply for weak B_z north.

The *AL* and *AE* indices have been shown to be strongly correlated to B_z and V_{sw} [*Maezawa*, 1979; *Murayama*, 1982; *Baker*, 1986, and references therein]. As substorm indices, *AE* and *AL* are most valuable during periods of B_z south when the enhanced auroral electrojet currents are in close proximity to the ground stations measuring their corresponding magnetic perturbations. However, during periods of B_z north, the electrojets diminish and the region of enhanced magnetic activity typically moves poleward beyond the effective range of the ground stations. Thus if one relies solely on the *AE* index as the monitor of solar wind–magnetospheric coupling, one is lead to model the magnetosphere as a half-wave rectifier where energy coupling proceeds for B_z south but turns off for B_z north.

Field-aligned current systems also indicate a strong dependence on IMF B_z. It has been shown [*Zanetti and Potemra*, 1986] that the integrated current intensity of the dayside auroral region 1 current system maximizes for strong B_z negative and decreases to a minimum for weak B_z positive, at which point the "NBZ" field-aligned currents develop poleward of the auroral oval and increase with increasing positive B_z. These NBZ currents characterize the polar cap arc state, and they can be extremely large at times [*Iijima and Shibaji*, 1987; *Rich et al.*, 1990]. *Gussenhoven* [1982] has shown that polar cap arcs, as viewed from auroral satellite images, occur preferentially (and with greater intensity) during periods of B_z north and large V_{sw}.

The variation of auroral boundaries with solar wind parameters also provides information on the effects of the solar wind on magnetosphere dynamics. Precipitating electrons have been used to define various auroral boundaries [*Hardy et al.*, 1982] which map to dynamically distinct magnetospheric regions: the equatorward boundary maps to the inner edge of the central plasma sheet, the transition boundary maps to the transition between the plasma sheet and the boundary layer, and the poleward boundary maps to the furthest extent in the magnetotail lobes that accelerated boundary layer electrons are found. *Hardy et al.* [1981] examined the relation between the electron equatorward boundary and the solar wind parameters (B_z, $V_{sw}B_z$) and found an expanding oval for increasingly negative B_z but no systematic variation for $B_z > 1$ nT. *Makita et al.* [1983] found that all three boundaries systematically moved equatorward for an increasing magnitude of B_z negative. However, for an increasing magnitude of B_z positive, only the movement of the poleward boundary toward higher latitudes was moderately well correlated. *Makita et al.* [1988] found that soft electron precipitation (i.e., average energy of less than 0.5–1 keV) mapping to boundary plasma regions is enhanced for periods of strong B_z north relative to weak B_z north.

The total hemispheric energy and number flux of precipitating electrons and ions is an important low-altitude measure of magnetospheric activity in that by its global nature it is biased toward neither the active oval (B_z south) nor the active polar cap (B_z north). *Foster et al.* [1986] have statistically determined precipitating electron hemispheric energy flux as a function of B_z. However, they did not consider V_{sw} dependence and, owing to their two B_z bin intervals ($B_z < -3$ nT; $B_z > +3$ nT), were unable to test for minimum precipitation levels at low B_z values. By including V_{sw} as a sorting parameter, increasing the B_z interval to include lower absolute magnitudes of B_z and analyzing ions as well as electrons, we extend the work of Foster and coworkers in using auroral precipitation as an important probe of magnetospheric dynamics.

This paper is divided into seven sections. Following the introduction (section 1), we present in section 2 the instrument and data coverage; in section 3, the data binning procedures; and in section 4, the derivation of hemispheric fluxes from the average spectra. The results are presented in section 5 and discussed in section 6. Section 7 is the summary and conclusion.

2. Instrumentation and Data Coverage

The data analyzed in this study are the particle fluxes measured by the SSJ/4 ion and electron detectors flown on the F6 and F7 satellites of the Defense Meteorological Satellite Program (DMSP). The time period of F6 data coverage includes January 1983 to July 1987, and for F7, December 1983 to July 1987. The DMSP satellites are continuously maintained in circular, polar, sun-synchronous orbits at an altitude of 840 km and an inclination of 98.3°. One orbit (F6) lies in the 0640–1840 magnetic local time (MLT) meridian plane, and the other (F7) lies in the 1030–2230 MLT meridian plane. The satellites are three-axis stabilized with the SSJ/4 sensor apertures oriented toward the local zenith at all times to measure precipitating particles.

The SSJ/4 detectors on each satellite consist of an array of four electrostatic analyzers that together measure electrons and ions over an energy range of 30 eV to 30 keV in 20 channels logarithmically spaced in energy. A 20-point spectrum is returned each second for both electrons and ions. A complete description of the SSJ/4 instrument is given by *Hardy et al.* [1984]. The instruments were extensively calibrated prior to flight and cross-calibrated in flight.

Although both DMSP satellite orbits are sun synchronous, each day they sweep out a wide range in corrected geomagnetic latitude (MLAT) and magnetic local time (MLT) coordinates owing to the offset between geographic and geomagnetic poles in combination with the Earth's rotation. Figure 1 shows the data coverage (combined hemispheres) in MLAT-MLT coordinates resulting from hundreds of DMSP F6 and F7 orbits. MLAT is marked in 10° increments from 50° to 90° by the concentric circles. The dots along the 50° MLAT circle appear every 0.5 hour in MLT. Coverage of the auroral region is nearly complete, with a data gap at low magnetic latitudes in the postnoon and postmidnight local time sectors.

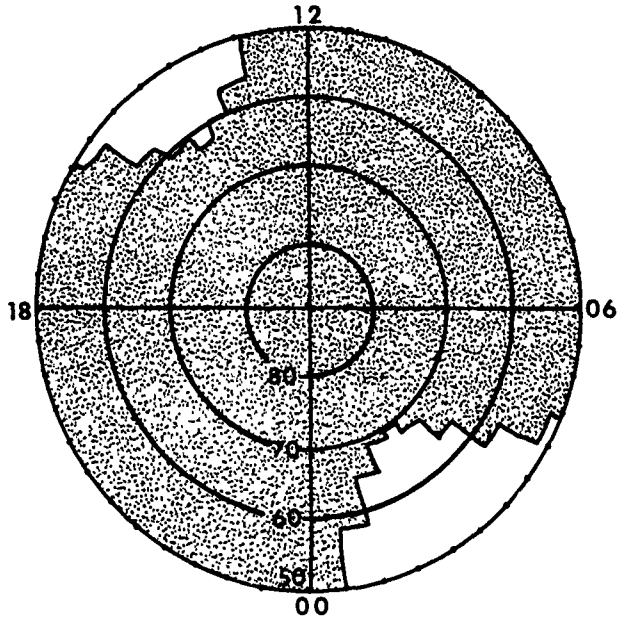

Fig. 1. The data coverage from DMSP F6 and F7 satellites for combined hemispheres displayed in a corrected geomagnetic latitude–magnetic local time coordinate system.

3. Data Binning Procedure

We have constructed identically structured but separate data bases for both electrons and ions. Our procedure for binning and averaging the data is identical to that of papers 1 and 2 except that instead of sorting the data by the *KP* index, we sort it by paired values of IMF B_z (in geocentric solar magnetospheric coordinates) and V_{sw}. The matrix of sorting parameters has six divisions in B_z ranging from −10 to +10 nT and five divisions in V_{sw} ranging from 200 to 800 km/s, resulting in 30 paired ranges of interplanetary parameters. The bin intervals for B_z and V_{sw} are listed in Table 1. Particle spectra sorted into each of the 30 categories are further ordered into a spatial grid (map) in corrected geomagnetic latitude (MLAT) and local time (MLT). The resolution of the map is 2° for 50°–60° and 80°–90° MLAT and 1° for 60°–80° MLAT; it is 0.5 hour in MLT. The magnetic coordinates are determined by mapping the satellite coordinates down to 100 km using the International Geophysical Reference Field (1982) and the Jensen-Cain magnetic field models.

Previous work [*Baker et al.*, 1983, and references therein] has shown that interplanetary parameters are most highly correlated with magnetospheric activity parameters when a time delay is assumed. This time delay ranges from 0.25 to 1 hour depending on the level of activity in the interplanetary medium and can be explained in terms of the propagation time of solar wind perturbations as well as the finite response time of the magnetosphere. A study we performed using 1826 hours of data showed that ordering 1-hour averages of the *AE* index by B_z and V_{sw} gives less scatter for 1-hour than for 0-hour lag time. We therefore chose a 1-hour time lag between the hourly averaged interplanetary data obtained from the National Space Science Data Center (NSSDC) data base [*Couzens and King*, 1986, 1989] and the precipitating particle data. Because the particle data resolution is 1 s, the stated time lag of 1 hour is used in an average sense only. For each hour a pair of IMF B_z and V_{sw} values exist; all 1-s particle spectra in the following 1-hour interval are sorted according to that pair of hourly averaged interplanetary parameters.

TABLE 1. Bin Intervals

B_z, nT		V_{sw}, km/s	
Interval	Average	Interval	Average
−10.0–−3.0	−4.8	200–375	346
−3.0–−1.5	−2.2	375–450	408
−1.5–0.0	−0.7	450–525	485
0.0–+1.5	+0.7	525–625	572
+1.5–+3.0	+2.1	625–800	677
+3.0–+10.0	+4.5		

Simultaneous IMF and plasma data were available for approximately two thirds of time between January 1983 and July 1987, resulting in a total of 13,263 pairs of hourly values. The data bases for electrons and ions each contain a total of 34 million spectra distributed between the 30 individual maps, each map consisting of between 0.2 and 2.7 million spectra. The average spectrum in each spatial bin is derived from hundreds to thousands of 1-s spectra sampled from tens to hundreds of individual passes. Within a given bin the independence between individual 1-s spectra varies widely with their temporal proximity to one another. The large number of separate passes contributing to each bin minimizes the impact that the autocorrelation between temporally clustered 1-s spectra may have on the average spectrum.

Table 2 summarizes the bin statistics and parameterization. Included for each of the 30 separations are the total number of spectra used in each map and the number of paired hourly values of B_z and V_{sw} along with their averages and standard deviations (σ). The table is arranged so that the six B_z bins are listed repeatedly for increasing values of V_{sw}. To simplify the bookkeeping, a single weighted average value of each of the B_z bins was used independently of V_{sw}. Likewise, a single value for each of the V_{sw} bins was used independently of B_z. These average bin values are listed in Table 1, along with their corresponding bin intervals. The differences between these averages and the averages listed in Table 2 are minor and inconsequential to the final results. Also included in Table 2 are the average values of *Kp* and the solar wind dynamic pressure associated with each map. The average *Kp* values will be used in a later section for comparing the current work to our previous *Kp* statistical studies (papers 1 and 2). The average dynamic pressure (proton mass times solar wind density times V_{sw} squared) has been determined from the NSSDC data base and will be referred to in the discussion (section 6).

Two points should be made concerning the map separations. One is that the extreme B_z negative and positive bins (7 nT wide) are much larger than the four moderate B_z bins (1.5 nT wide). These wide bins were necessitated by the paucity of strong B_z conditions and the requirement for adequate bin statistics. For these wide bins the resulting standard deviations in B_z are about 3 times those found in the four moderate B_z bins (see Table 2). The second point is that there is an apparent minimum number of spectra required to produce a smoothly varying and statistically significant map. We find this number to be between 0.25 and 0.5

TABLE 2. Bin Averages and Statistics

Map Number	Spectra, $\times 10^6$	Hours	B_z, nT		V_{sw}, km/s		Kp		P_k, keV/cm^3	
			Average	Sigma	Average	Sigma	Average	Sigma	Average	Sigma
	0.81	290	−4.5	1.3	346.	20.	2.8	0.8	21.6	10.1
2	1.20	405	−2.2	0.4	346.	20.	1.9	0.8	19.6	9.0
3	2.25	780	−0.7	0.4	345.	20.	1.4	0.8	18.5	8.3
4	2.25	811	0.7	0.4	345.	21.	1.1	0.8	18.1	8.2
5	1.40	501	2.1	0.4	347.	21.	1.1	0.8	17.8	8.6
6	1.02	360	4.5	1.4	349.	22.	1.3	0.9	20.4	9.1
7	1.12	441	−4.9	1.5	408.	21.	3.6	1.1	22.1	11.9
8	1.45	532	−2.2	0.4	409.	21.	2.7	0.9	19.0	10.1
9	1.60	923	−0.8	0.4	408.	21.	2.0	0.9	17.9	10.7
10	2.66	1,007	0.7	0.4	409.	21.	1.7	0.9	17.1	9.6
11	1.92	697	2.1	0.4	408.	20.	1.6	0.9	17.9	9.1
12	1.52	562	4.6	1.5	407.	21.	1.8	1.1	22.5	13.9
13	0.72	311	−5.0	1.7	485.	22.	4.3	1.1	26.9	16.1
14	0.80	332	−2.2	0.4	485.	22.	3.2	0.8	19.3	10.9
15	1.38	553	−0.7	0.4	484.	23.	2.7	0.9	17.7	8.5
16	1.65	653	0.7	0.4	484.	22.	2.2	1.1	17.3	10.8
17	1.13	421	2.1	0.4	487.	22.	2.0	1.2	17.5	11.2
18	0.86	348	4.7	1.7	486.	20.	2.4	1.2	25.8	14.3
19*	0.42	197	−4.7	1.5	569.	25.	4.6	1.0	27.7	13.3
20	0.61	255	−2.3	0.5	573.	29.	3.9	0.9	21.3	8.6
21	1.03	427	−0.7	0.4	572.	28.	3.4	1.1	20.5	9.2
22	1.23	502	0.7	0.4	573.	28.	2.9	1.0	19.0	8.2
23	0.98	410	2.1	0.4	571.	28.	2.6	1.1	19.3	8.3
24	0.65	284	4.4	1.4	572.	29.	3.0	1.2	26.2	13.4
25*	0.16	71	−4.4	1.4	668.	36.	5.0	1.1	25.9	11.1
26*	0.35	149	−2.2	0.4	675.	40.	4.4	0.9	23.3	10.3
27	0.66	256	−0.8	0.4	679.	44.	3.9	0.9	22.1	7.7
28	0.87	368	0.7	0.4	679.	42.	3.5	0.9	21.1	8.0
29	0.63	261	2.2	0.4	675.	38.	3.2	1.0	21.8	10.3
30*	0.42	156	4.3	1.3	677.	36.	3.0	1.2	27.3	15.9
	33.75†	13,263†								

*Maps omitted from study.
†Totals.

million spectra, the exact level depending on the intrinsic variability of the data, which in turn depends on the activity and the width of the bins. We note that maps 19, 25, 26, and 30 consist of fewer than 0.5 million spectra each, with the majority of their average spectra defined by less than 10 passes of data and representing an insignificant number of truly independent 1-s spectra. Of these maps, all but number 26 correspond to a wide B_z bin which compounds the difficulty of providing meaningful average hemispheric fluxes. Therefore aside from including the data from these four maps in Tables 2 and 3, they have been omitted from the study.

4. Definition of Average Spectral Moments

Average spectra are determined from the 1-s spectra accumulated in each spatial bin for each map. From these average spectra (combined north and south poles), we determine for both ions and electrons the total precipitating number and energy flux into the hemisphere each second under different average interplanetary conditions. To provide the best estimate of the total hemispheric particle flux input in the statistical results presented here, we fill the data gaps indicated in Figure 1 by interpolation. Upon examination of the flux maps created in this study (not shown), it is found that flux levels adjacent to the data gap in the postmidnight sector are above backround for ≥58° MLAT. At these latitudes, interpolation between real flux data is limited to ≤2.5 hours in MLT. Fluxes adjacent to the postnoon sector data gap are at backround level, and interpolation across the gap is of no consequence to the final results.

In about 30% of the average ion (electron) spectra, particularly those determined for high levels of geomagnetic activity on the evening (morning) side of the oval, a substantial portion of the high-energy tail of the spectra lies beyond the 30-keV upper bound of the SSJ/4 instrument. This can underestimate (more significantly for ions than electrons) the total precipitating integral number and energy flux. To correct for this, we selectively extrapolate average spectra to three additional logarithmically spaced energies (45, 65, 90 keV) assuming the tails of the spectra to be Maxwellian extensions of the high-energy measurements (see paper 2 for a detailed discussion of this conservative correction).

From the average spectra we calculate the integral energy flux (E_{FLUX} in keV/s cm^2 sr) and integral number flux (N_{FLUX} in particles/s cm^2 sr) using the equations

$$E_{\mathrm{FLUX}} = E_1 \cdot j(E_1) \cdot (E_2 - E_1) + \sum_{k=2}^{22} E_i \cdot j(E_i) \cdot \frac{(E_{i+1} - E_{i-1})}{2} + E_{23} \cdot j(E_{23}) \cdot (E_{23} - E_{22}) \quad (1)$$

$$N_{\mathrm{FLUX}} = j(E_1) \cdot (E_2 - E_1) + \sum_{i=2}^{22} j(E_i) \cdot \frac{(E_{i+1} - E_{i-1})}{2} + j(E_{23}) \cdot (E_{23} - E_{22}) \quad (2)$$

where $j(E_i)$ is the differential ion or electron number flux in units of particles/(cm^2 s sr keV) for the ith energy channel and E_i is the central energy in units of keV. The summation runs over the 20 measured channels plus the three extrapolated channels. We integrate N_{FLUX} and E_{FLUX} over each spatial map (i.e., above 50° MLAT) to obtain for each of the 30 average interplanetary conditions the precipitating particle hemispheric integral number flux ($H_{N_{\mathrm{FLUX}}}$, in particles/(s sr)) and hemispheric integral energy flux ($H_{E_{\mathrm{FLUX}}}$, in gigawatts). As in paper 2, we assume that the precipitating particle distributions are isotropic and thus introduce a factor of pi in converting $H_{E_{\mathrm{FLUX}}}$ to gigawatts. Throughout the text we use the convention of preceding N_{FLUX} and E_{FLUX} with an "H" when referring to the spatially integrated hemispheric flux.

Approximately 30% of the average ion and electron spectra were extrapolated. In the majority of the extrapolated ion spectra, the E_{FLUX} was increased by less than 50%, while the N_{FLUX} increased by less than 10%. The effect of extrapolation on the electron spectra is less significant with the E_{FLUX} increasing by less than 20% and the N_{FLUX} increasing by less than 10%. These increases in integral fluxes for individual spectra translate to a 5–90% (0–9%) increase in the ion (electron) hemispheric energy flux and a 1–12% (0–0.4%) increase in the ion (electron) hemispheric number flux, depending on activity level. In listing hemispherically integrated values, both those from unextrapolated and extrapolated spectra are given.

For additional details on data reduction techniques (cross-satellite normalization, smoothing, and extrapolation), we refer the reader to papers 1 and 2.

5. Results

The spatial patterns in the E_{FLUX} and N_{FLUX} maps generated in this study are similar to those shown previously in papers 1 and 2; only the quantitative details differ. We therefore refer the reader to the previous papers for a discussion of the morphological features of auroral precipitation, and in this paper we concentrate on the total hemispheric energy and number flux for the precipitating ions and electrons and their dependence on the solar wind speed and the IMF B_z component. Independent of the spatial distribution over the auroral zone of the energy and number flux, we take the integrated hemispheric inputs ($H_{E_{\mathrm{FLUX}}}$ and $H_{N_{\mathrm{FLUX}}}$) to be a measure of the character and strength of the solar wind–magnetosphere coupling. Detailed analysis of the dependence of the precipitation patterns and the average spectra on V_{sw} and IMF B_z, especially as they pertain to the various auroral regions such as the boundary layers and the central plasma sheet, will be addressed in a future paper.

5.1. *Hemispheric Flux as a Function of B_z and V_{sw}*

The $H_{E_{\mathrm{FLUX}}}$ and $H_{N_{\mathrm{FLUX}}}$, as determined by integrating the extrapolated average spectra over the spherical area of the auroral region, are listed in Table 3 and plotted in Figures 2–5. The fluxes determined from the unextrapolated spectra are also included in parentheses in Table 3. In Figures 2–5 the electron results are plotted on the left, and the ion results are shown on the right. All scales are linear. The hemispheric number flux plots have different multiplicative factors for electrons (10^{25}) and ions (10^{23}). We have plotted the data in two ways to illustrate the two principal characteristics of the B_z and V_{sw} variation. $H_{N_{\mathrm{FLUX}}}$ and $H_{E_{\mathrm{FLUX}}}$ are plotted against B_z for fixed V_{sw} in Figures 2 and 3, respectively, and are plotted against V_{sw} for fixed B_z in Figures 4 and 5, respectively. Different symbols, as defined in the symbol key, are used for each different B_z and V_{sw} case. As was previously mentioned in section 3, values from four of the initial 30 maps have been omitted and will not be used in any of the following analyses owing to their poor statistics.

The electron and ion hemispheric number flux (Figure 2) and ion hemispheric energy flux (Figure 3) vary similarly with B_z: decreasing from an absolute maximum for strong B_z negative to a minimum for weak to moderate B_z positive, followed by an increase to a second maximum for strong B_z positive. The electron hemispheric energy flux (Figure 3) falls off rapidly from its maximum for strong B_z negative to weak B_z positive, gradually leveling off to its minimum for strong B_z positive. The electron and ion energy fluxes show the largest overall increase from their minimum to their maximum for strong B_z negative, by a factor of 5.8 and 3.7, respectively. This occurs for the lowest V_{sw} bin, with the factors decreasing for higher V_{sw}. The electron and ion number fluxes show smaller rises, both increasing by a factor of approximately 2.5 and remaining near this value for all V_{sw}. For B_z positive of the minimum, all but the electron $H_{E_{\mathrm{FLUX}}}$ increase. The increase is largest for the ions with an average rise of a factor of 1.41 and 1.42 for the ion $H_{E_{\mathrm{FLUX}}}$ and $H_{N_{\mathrm{FLUX}}}$, respectively. The electron $H_{N_{\mathrm{FLUX}}}$ increases on average by a factor of 1.19.

Figures 4 and 5 illustrate that for each B_z value the four hemispherically integrated fluxes exhibit a near-linear variation with V_{sw}. Again the electron and ion $H_{E_{\mathrm{FLUX}}}$ show the largest variation, increasing by an average factor of 4.08 and 2.11, respectively, over the full velocity range. The electron and ion $H_{N_{\mathrm{FLUX}}}$ increase by a factor of 1.82 and 1.16, respectively.

The similarity in the variation of the four quantities with B_z and V_{sw} suggests that the variation can be fit by either of two relatively simple functional forms. In each case, the B_z functionality is modeled by a parabolic least squares fit to the data, and the V_{sw} functionality, by a linear least squares fit. In the first case, the two functions are summed:

$$f(B_z, V_{sw}) = a(B_z - b)^2 + [cV_{sw} + d] \quad (3)$$

while in the second case, they are multiplied:

$$f(B_z, V_{sw}) = [a(B_z - b)^2 + 1][cV_{sw} + d]. \quad (4)$$

Although equations (3) and (4) have four free parameters each, the functional forms differ. Equation (3) is the simpler,

TABLE 3. Hemispheric Fluxes (Electron and Ion)

Map Number	B_z, nT	V_{sw}, km/s	Electron $H_{E_{FLUX}}$, GW	Electron $H_{N_{FLUX}}$, $\times 10^{25}$ (s sr)$^{-1}$	Ion $H_{E_{FLUX}}$, GW	Ion $H_{N_{FLUX}}$, $\times 10^{23}$ (s sr)$^{-1}$
1	−4.5	346.	35.00 (34.50)	3.83 (3.83)	3.71 (2.63)	7.03 (6.61)
2	−2.2	346.	20.80 (20.50)	2.68 (2.68)	2.19 (1.77)	4.78 (4.61)
3	−0.7	346.	11.80 (11.70)	2.01 (2.01)	1.37 (1.20)	3.65 (3.58)
4	0.7	346.	7.18 (7.17)	1.74 (1.74)	1.18 (1.05)	3.65 (3.60)
5	2.2	346.	5.71 (5.70)	1.65 (1.65)	1.02 (0.96)	3.60 (3.58)
6	4.5	346.	6.23 (6.17)	2.01 (2.01)	1.38 (1.28)	5.44 (5.39)
7	−4.5	408.	49.50 (48.50)	5.05 (5.04)	5.05 (3.16)	8.10 (7.39)
8	−2.2	408.	26.80 (26.40)	3.03 (3.03)	2.56 (1.83)	4.88 (4.60)
9	−0.7	408.	18.60 (18.40)	2.55 (2.55)	1.93 (1.49)	4.01 (3.84)
10	0.7	408.	11.50 (11.40)	2.04 (2.04)	1.56 (1.23)	3.55 (3.42)
11	2.2	408.	9.58 (9.54)	2.08 (2.08)	1.36 (1.19)	3.82 (3.75)
12	4.5	408.	8.82 (8.79)	2.41 (2.41)	1.78 (1.55)	5.35 (5.26)
13	−4.5	485.	65.90 (63.30)	5.87 (5.86)	5.72 (3.21)	8.62 (7.71)
14	−2.2	485.	37.60 (36.50)	3.54 (3.54)	2.68 (1.76)	4.83 (4.48)
15	−0.7	485.	27.40 (26.90)	2.87 (2.87)	2.09 (1.45)	3.87 (3.62)
16	0.7	485.	15.90 (15.80)	2.30 (2.30)	1.86 (1.30)	3.61 (3.40)
17	2.2	485.	12.80 (12.70)	2.23 (2.23)	1.52 (1.23)	3.60 (3.48)
18	4.5	485.	11.60 (11.50)	2.77 (2.77)	2.21 (1.79)	5.46 (5.30)
19*	−4.5	572.	68.40 (64.60)	5.93 (5.92)	5.70 (3.05)	8.53 (7.58)
20	−2.2	572.	46.90 (44.70)	4.07 (4.06)	3.31 (1.98)	5.74 (5.25)
21	−0.7	572.	38.80 (37.40)	3.54 (3.54)	2.83 (1.65)	4.64 (4.21)
22	0.7	572.	25.40 (24.70)	2.87 (2.86)	2.30 (1.41)	3.78 (3.45)
23	2.2	572.	18.70 (18.30)	2.77 (2.77)	1.89 (1.32)	3.60 (3.38)
24	4.5	572.	18.00 (17.80)	3.18 (3.18)	2.85 (1.95)	5.48 (5.15)
25*	−4.5	677.	65.50 (60.00)	5.42 (5.40)	4.61 (2.27)	6.64 (5.86)
26*	−2.2	677.	60.20 (55.20)	4.66 (4.64)	3.28 (1.89)	5.64 (5.13)
27	−0.7	677.	43.50 (41.10)	3.82 (3.81)	2.86 (1.64)	4.66 (4.22)
28	0.7	677	36.30 (34.70)	3.49 (3.48)	2.42 (1.42)	3.99 (3.63)
29	2.2	677.	25.00 (24.30)	3.11 (3.11)	2.36 (1.43)	4.04 (3.70)
30*	4.5	677.	20.30 (19.80)	3.13 (3.13)	2.76 (1.77)	4.85 (4.49)

Unextrapolated values are listed in parentheses.
*Maps omitted from study.

containing only the terms B_z^2, B_z, and V_{sw}. Equation (4) contains the additional cross terms, $V_{sw}B_z$ and $V_{sw}B_z^2$. The four constants, a through d, for the two methods of fitting are listed in Table 4. Because there are four free parameters in each method, the quality of fit should be approximately the same. A quantitative comparison between the hemispheric fluxes listed in Table 3 and those calculated by applying the fit coefficients in Table 4 (methods 1 and 2) to

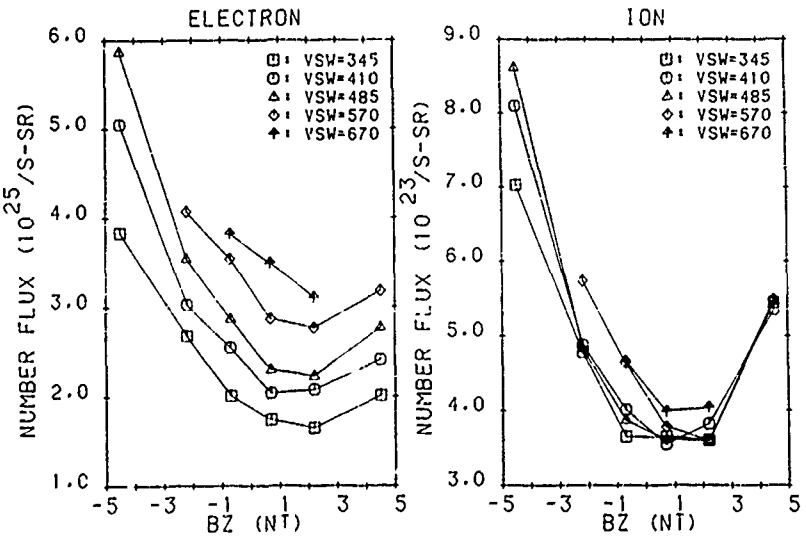

Fig. 2. The hemispheric number flux ($H_{N_{FLUX}}$), in particles/(s sr), plotted as a function of the bin-averaged value of IMF B_z. (Left) Electrons. (Right) Ions.

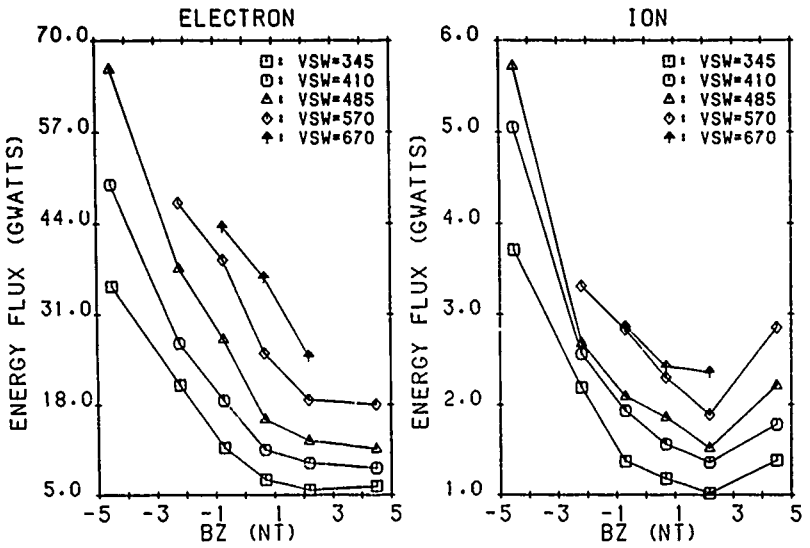

Fig. 3. The hemispheric energy flux ($H_{E_{FLUX}}$), in gigawatts, plotted as a function of the bin-averaged value of IMF B_z. (Left) Electrons. (Right) Ions.

equations (3) and (4), respectively, show the following: Method 1 results in 71% (94%) of the hemispheric fluxes being fit to within 10% (20%) of the data. The correlation coefficient for a linear regression run between the data and fitted points for each category of fluxes ($H_{E_{FLUX}}$ and $H_{N_{FLUX}}$ for both electrons and ions) averaged 0.95. Method 2 yielded slightly better fits, with 80% (99%) of fitted points within 10% (20%) of the data. The average correlation coefficient for method 2 was 0.98. A more detailed discussion of the fitting methods and results are provided as an appendix to this report.

5.2. *Comparison of Ion and Electron Hemispherically Integrated Fluxes*

A cursory examination of Table 3 shows that the ion $H_{E_{FLUX}}$ ($H_{N_{FLUX}}$) is always less than the electron $H_{E_{FLUX}}$ ($H_{N_{FLUX}}$) by about 1 (2) orders of magnitude. However, a closer examination of the ratios between ion and electron hemispheric fluxes ($H_{E_{FLUX}}$ and $H_{N_{FLUX}}$) show important variations with respect to B_z and V_{sw}. Figure 6 left (right) shows the ratio of ion to electron $H_{E_{FLUX}}$ ($H_{N_{FLUX}}$) plotted as a function of B_z for fixed V_{sw}.

The largest ratio (0.22) of ion to electron $H_{E_{FLUX}}$ (e.g., when the two are most comparable) occurs for the lowest velocities and for B_z strongly northward. The ratio decreases sharply as B_z decreases toward zero and levels off to an approximately constant value for B_z negative. This trend occurs at each velocity level. The ratios vary in total by a factor of 4 from 0.054 to 0.223. For a fixed B_z the ratio decreases with increasing velocity in a roughly linear manner. The rate of decrease is greater for B_z positive than for B_z negative.

A comparable variation is seen in the $H_{N_{FLUX}}$ ratio. The largest values are seen for the lowest velocity and the largest

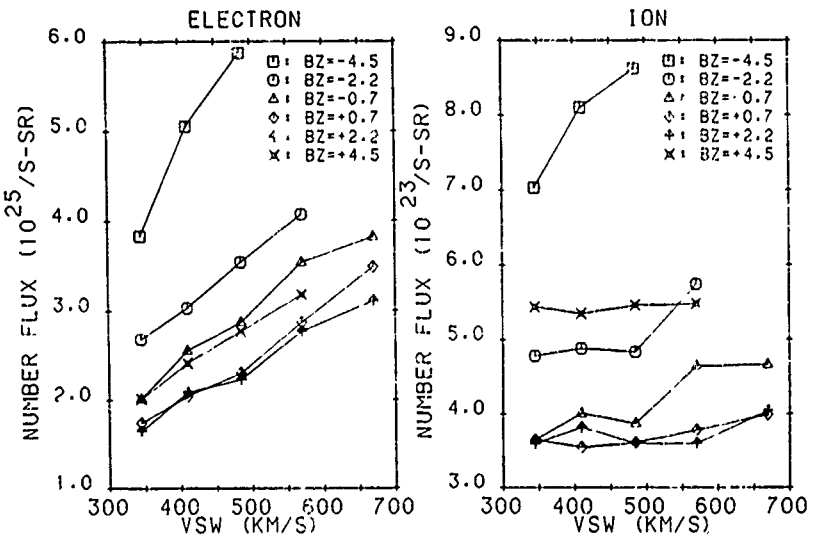

Fig. 4. The hemispheric number flux ($H_{N_{FLUX}}$), in particles/(s sr), plotted as a function of the bin-averaged value of V_{sw}. (Left) Electrons. (Right) Ions.

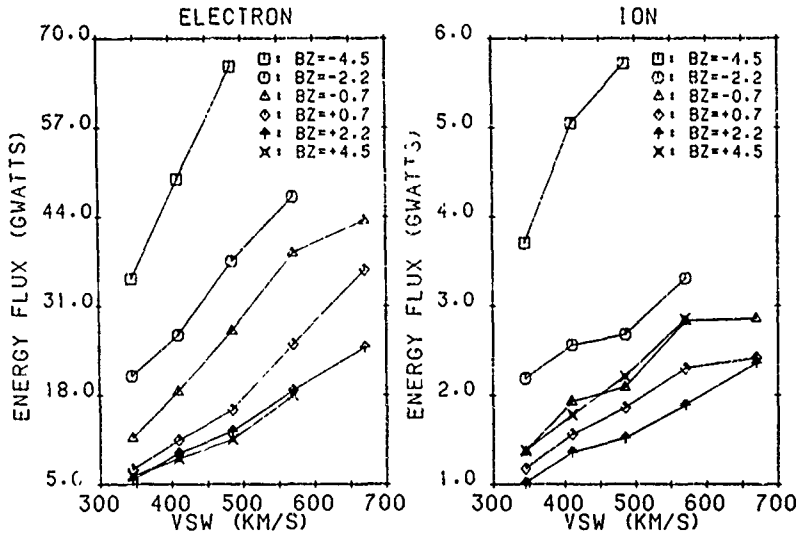

Fig. 5. The hemispheric energy flux ($H_{E_{FLUX}}$), in gigawatts, plotted as a function of the bin-averaged value of V_{sw}. (Left) Electrons. (Right) Ions.

B_z positive. For B_z positive the value decreases rapidly for decreasing B_z for all V_{sw}. For B_z negative the value is approximately constant for a given V_{sw}. Again there is a larger variation with velocity for B_z positive than for B_z negative.

5.3. *Variation of Kp With B_z and V_{sw}*

As a point of comparison to our previous studies, we have used 3-hour Kp averages to determine the variation in Kp with B_z and V_{sw} for the data set used here. Similar studies of magnetic activity variation with solar wind parameters have been performed, and those that most closely parallel this analysis are given by *Berthelier* [1976] and *Maezawa and Murayama* [1986]. The results are tabulated in Table 2 and plotted in Figure 7, where the separations in B_z and V_{sw} are the same as for the $H_{E_{FLUX}}$ and $H_{N_{FLUX}}$ studies. One notes that Kp exhibits the same general variation with B_z and V_{sw} as do $H_{E_{FLUX}}$ and $H_{N_{FLUX}}$. Kp has a minimum value for B_z weak to moderately positive and increases slightly for B_z strongly positive. Kp increases approximately linearly with V_{sw}. This similarity in behavior is not surprising, since Kp should respond to the general level of geomagnetic activity in the oval, which in turn should be proportional to the total number and energy flux input into the oval.

Figure 7 also shows that any separation of the data by Kp will mix periods of different polarity in B_z and have a broad range in V_{sw}. In Figure 8 we show the distribution of B_z for Kp = 0, 2, 4, and 6, over the same time period from which our data base is made. Plotted, for four Kp levels, is the fraction of time that B_z falls within each of 1.5-nT-wide bins over the range −10.5 to +10.5 nT. The figure illustrates that even for low activity (Kp = 0), the IMF B_z component is negative 12% of the time. Conversely, for very active periods (Kp = 6), the IMF B_z component is positive 23% of the time. For more moderate periods (Kp = 2 and Kp = 4) the percentage of opposite B_z polarities is approximately equal. Thus a separation by Kp poorly reflects groupings of those solar wind parameters that order the degree of the solar wind–magnetospheric coupling.

6. DISCUSSION

We have shown that the average hemispheric input of particle energy and particle flux for precipitating electrons

TABLE 4. Hemispheric Flux Fit Coefficients

	Electrons		Ions	
Coefficient*	Energy Flux	Number Flux	Energy Flux	Number Flux
		Method 1		
a, x/nT^2	0.59	0.06	0.07	0.14
b, nT	4.45	2.33	2.00	0.96
c, x/(km/s)	0.092	0.005	0.004	0.002
d, x	−34.20	−0.31	−0.38	2.66
$-d/c$, km/s	372.	62.	95.	−1330.
		Method 2		
a, 1/nT	0.08	0.03	0.06	0.04
b, nT	3.31	2.00	1.88	0.95
c, x/(km/s)	0.041	0.004	0.004	0.001
d, x	−8.65	−0.21	−0.32	3.29
$-d/c$, km/s	211.	−53.	80.	−3290.

*Variable x is in gigawatts (energy flux) or (s sr)$^{-1}$ (number flux).

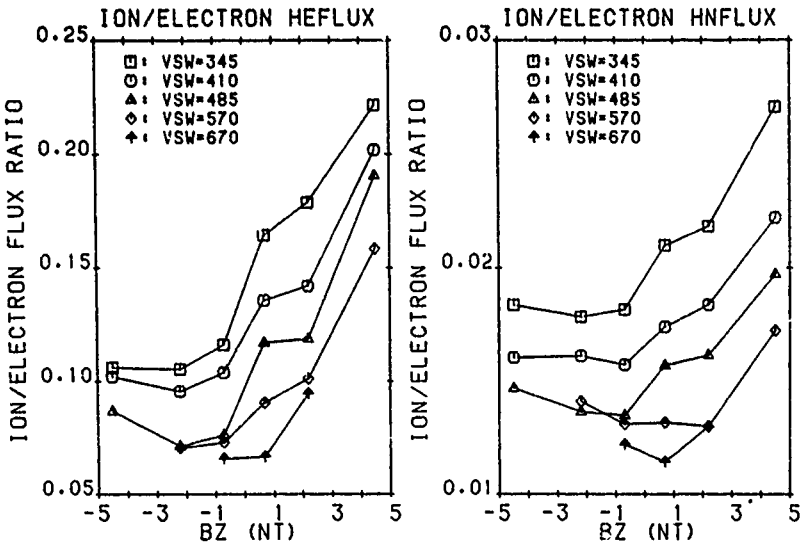

Fig. 6. The ratio of ion to electron hemispheric flux (left, $H_{E_{FLUX}}$; right, $H_{N_{FLUX}}$) plotted as a function of B_z.

and ions in the auroral region varies in a consistent and relatively simple manner with the magnitude of the IMF B_z component and with the solar wind velocity V_{sw}. In this section we examine the implications of these variations in more detail. Specifically, we address the following issues: (1) the statistical significance of the increase in $H_{E_{FLUX}}$ and $H_{N_{FLUX}}$ for large B_z positive, (2) the possible role of solar wind pressure in the increase for B_z positive, (3) the significance of the functional form that results from fitting the data, (4) the role of the solar wind velocity in controlling the energy transfer, and (5) the comparison of these results to earlier studies.

6.1. *Possible Bias in the B_z Distribution*

We first address whether the increase in $H_{E_{FLUX}}$ and $H_{N_{FLUX}}$ (predominantly for ions) for increasing B_z positive is a residual effect of preceding B_z negative intervals or is a real effect associated with strong B_z positive. *Nakai and Kamide* [1983] have shown that the magnetospheric response to B_z positive as measured by the motion of the equatorward boundary of the oval is much slower than for B_z negative. This implies that for several hours after a northward turning of B_z, the $H_{E_{FLUX}}$ and $H_{N_{FLUX}}$ could be affected in part by the residual influence of the increasingly more remote B_z negative time period. The only way this could explain the observed rise in $H_{E_{FLUX}}$ and $H_{N_{FLUX}}$ with increasing B_z positive would be if the probability that a period of large negative B_z prior to a period of positive B_z increases for increasing magnitude of positive B_z.

To investigate this, we used the IMF data covering the time period of 1983–1986. From this set we extracted those hourly B_z positive values which belonged to a time interval that had continuous coverage running backward in time to an hour where B_z fell below −2 nT. These cases were binned according to their magnitude (two bins defined by 0 to +3 nT, +3 to +10 nT), as well as by the number of hours (up to

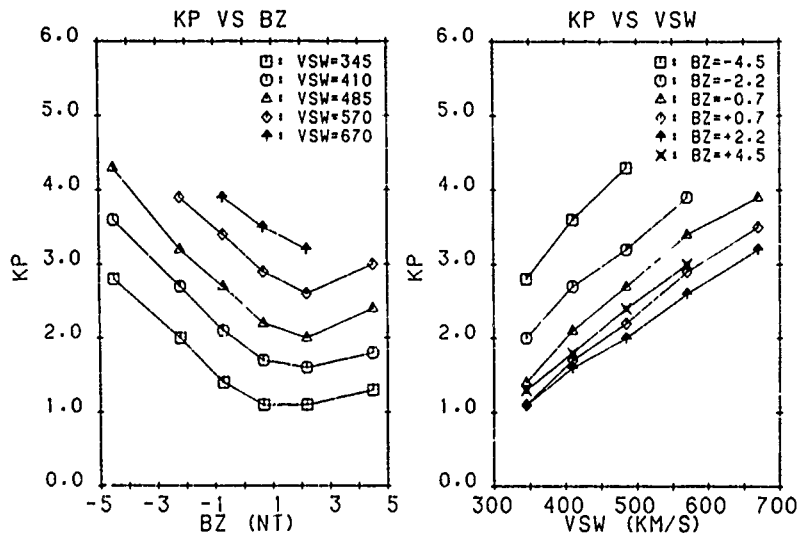

Fig. 7. The average value of Kp for each of the 26 bins (Table 2) plotted as a function of (left) bin-averaged B_z values and (right) bin-averaged V_{sw} values.

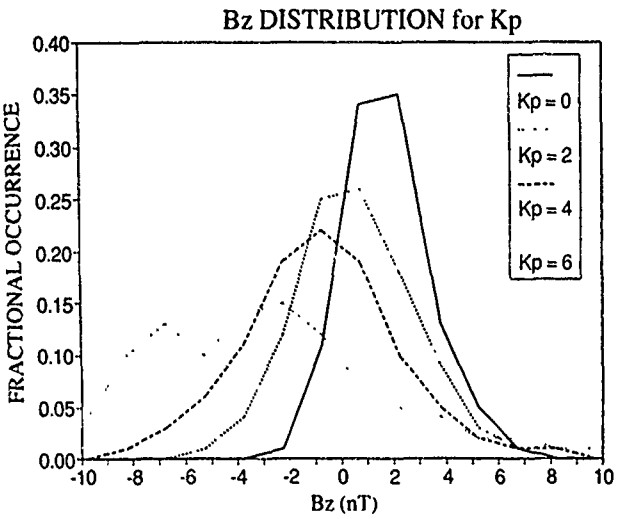

Fig. 8. Distribution of the fraction of time that B_z falls within each of the various B_z bins for $Kp = 0, 0+; 2-, 2, 2+; 4-, 4, 4+;$ and $\geq 6-$.

13) between them and the nearest preceding negative B_z. This sort resulted in 4032 (1418) hours in the weak (strong) B_z positive bin. The results of this analysis are plotted in Figure 9. Plotted as a function of the hours preceding a given B_z positive measurement for both B_z bins is the fraction of cases where a B_z of less than -2 nT occurred. For example, for a given hourly measurement of B_z positive (either weak or strong), the probability of encountering a B_z of less than -2 nT within the past 6 hours is around 63%. It is evident from the plot that there is no significant difference in B_z history for the two B_z positive bins used here. Thus the increase in hemispheric fluxes for strong B_z positive cannot be attributed to a residual effect due to previous B_z negative periods.

6.2. *Correlation of Hemispheric Fluxes and the Solar Wind Pressure*

The values of the solar wind dynamic pressure (mpV_{sw}^2) listed in Table 2 follow a similar trend with respect to B_z, as do the ion hemispheric fluxes. That is, the pressure approaches a minimum for small to moderately large B_z positive. One difference is that the pressure is more symmetric about its minimum, with more nearly equal pressure for both strong B_z south and strong B_z north. The increase in dynamic pressure, and subsequent compression of the magnetosphere, could partly explain the increase in total precipitating number and energy particle flux. This possibility is supported by the work of *Scurry and Russell* [1989]. They analyzed the activity index Am and the solar wind pressure during periods of northward B_z and concluded that the apparent correlation between geomagnetic activity and increasingly northward B_z is largely a side effect of increasing dynamic pressure during periods of large B_z.

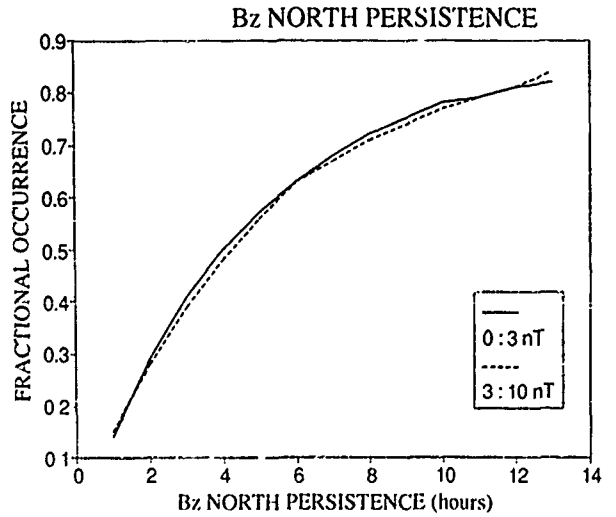

Fig. 9. A plot of the relative proximity of preceding B_z south intervals to both moderate and strong B_z north intervals.

6.3. *Fits to Data*

We have shown that for both electrons and ions, the variation of both the average hemispheric particle energy flux and the particle number flux with the solar wind velocity V_{sw} and IMF B_z component can be represented by equation (3) or (4). A large body of work exists on the nature of the solar wind-magnetosphere interactions. Many of these have been investigations of the relationship between some index reflecting the approximate level of geomagnetic activity and some combination of parameters in the solar wind. Typically, indices such as AE, AL, Kp, and Ap have been investigated as a function of $V_{sw}B_z$, $V_{sw}B_s$, $V_{sw}^2B_s$, and ε [*Baker et al.*, 1983, and references therein; *Bargatze et al.*, 1985]. In such studies, B_z is the average value of the north-south component of the IMF, while B_s is the value averaged only when B_z is southward. The parameter $\varepsilon = V_{sw}B^2 \sin^4(\Theta/2)l_0^2$, where Θ is given by $\tan^{-1}(B_y/B_z)$ or by this angle's supplement for $B_z < 0$ and l_0 is a constant. In many of these studies, the assumption has been that the magnetosphere operates as a half-wave rectifier with activity increasing steadily for increasingly negative B_z, but exhibiting negligible activity for increasingly positive B_z [*Burton et al.*, 1975].

The studies cited above have shown in general that $V_{sw}B_z$, $V_{sw}B_s$, $V_{sw}^2B_s$, and ε all provide approximately the same level of correlation with the various geomagnetic activity indices. Our function is somewhat similar to the epsilon function in that it has a linear dependence on V_{sw} and a quadratic dependence on B_z. Unlike the epsilon parameter, however, our functional form shows no strong gating with the IMF polarity, as would be required for a half-wave rectifier response. Rather, we show a minimum in particle precipitation for B_z weakly to moderately positive, with an increase for strong B_z positive. This is consistent with studies of other low-altitude signatures used to monitor magnetospheric activity. For B_z increasing from weak to strong positive values, *Reiff and Luhmann* [1986] have pointed to studies suggesting an increase in the cross-polar cap potential, *Gussenhoven* [1982] has found an increase in polar cap arc activity, *Zanetti and Potemra* [1986] point to the establishment and enhancement of "NBZ" currents in the polar region, and *Makita et al.* [1988] have shown an enhancement of the soft electron boundary plasma at very high latitudes. These studies all show that the magnetosphere becomes energized through mechanisms driven by B_z positive as well as by B_z negative.

TABLE 5. Efficiency of V_{sw} for B_z South and North

	$H_{E_{FLUX}}$, GW				$H_{N_{FLUX}}$, (s sr)$^{-1}$			
	Electron		Ion		Electron, $\times 10^{25}$		Ion, $\times 10^{23}$	
V_{sw}, km/s	B_{zs}	B_{zn}	B_{zs}	B_{zn}	B_{zs}	B_{zn}	B_{zs}	B_{zn}
346	18.6	6.5	2.0	1.2	2.5	1.8	4.6	4.0
677	50.7	29.1	3.0	2.4	4.3	3.3	5.1	4.2
Ratios	2.7	4.5	1.5	2.0	1.7	1.8	1.1	1.1

6.4. *Efficiency of V_{sw} in Controlling Energy Transfer*

Rossberg [1984] showed that during periods of B_z north, AE increases linearly with V_{sw}. In his subsequent work [*Rossberg*, 1989], he examined the variation of the magnetic activity index AL for both B_z south and B_z north during intervals of both low V_{sw} (<400 km/s, with an average of 358 km/s) and high V_{sw} (>700 km/s, with an average of 740 km/s). For periods of both B_z south (B_{zS}) and B_z north (B_{zN}), he determined the ratios of AL for high and low V_{sw}. From these ratios, he concluded that the solar wind speed dependent processes involved in solar wind–magnetosphere coupling are twice as efficient in their transfer of energy during periods of B_z north than periods of B_z south.

We assume that the hemispheric energy flux of precipitating particles is at least as good as the AL index in providing a measure of the efficiency with which V_{sw} contributes to the energy transfer from the solar wind to the magnetosphere. Using this assumption, we follow an analysis similar to Rossberg's, substituting the hemispheric energy flux for AL. To provide the best comparison to Rossberg's results, we combined our data to determine the average value of the electron and ion $H_{E_{FLUX}}$ for B_{zS} and B_{zN} for the lowest (346 km/s) and highest (677 km/s) V_{sw} cases. These data, as well as the corresponding $H_{N_{FLUX}}$ data, are listed in Table 5. For all columns the flux ratios for the high-velocity case to the low-velocity case are given in the last row. Rossberg found that for B_{zS} (B_{zN}), a doubling of V_{sw} leads to an increase by a factor of 2.8 (5.9) in the average AL index. Our study gives a similar result in the average hemispheric electron flux for B_{zS} (B_{zN}). A doubling of V_{sw} leads to an increase by a factor of 2.7 (4.5). Thus both studies show that an increase in V_{sw} is most efficient in increasing magnetospheric activity during northward B_z. As is indicated in Table 5, the ion hemispheric energy flux exhibits a similar if somewhat less pronounced variation. Although there is a clear asymmetry in the efficiency of V_{sw} in transferring energy to the magnetosphere under the two different B_z polarities, such is not the case for the transfer of mass (number flux). There are no significant differences for B_z north and south in corresponding ratios for the average hemispheric number flux.

6.5. *Comparisons With Other Studies*

The majority of the statistical studies mapping out the region of precipitating particles have been ordered by the magnetic activity index Kp. For electrons, these include *Wallis and Budzinski* [1981], *Spiro et al.* [1982], *Hardy et al.* [1985], and *Foster et al.* [1986]; and for ions, *Hardy et al.* [1989]. *Brautigam et al.* [1988] compared the electron hemispheric energy flux from these studies and found excellent agreement.

As an indirect comparison of the hemispheric fluxes derived from our Kp statistical studies (papers 1 and 2) and those from the study presented here, we plot electron and ion hemispheric flux versus Kp, using the B_z:V_{sw} bin-

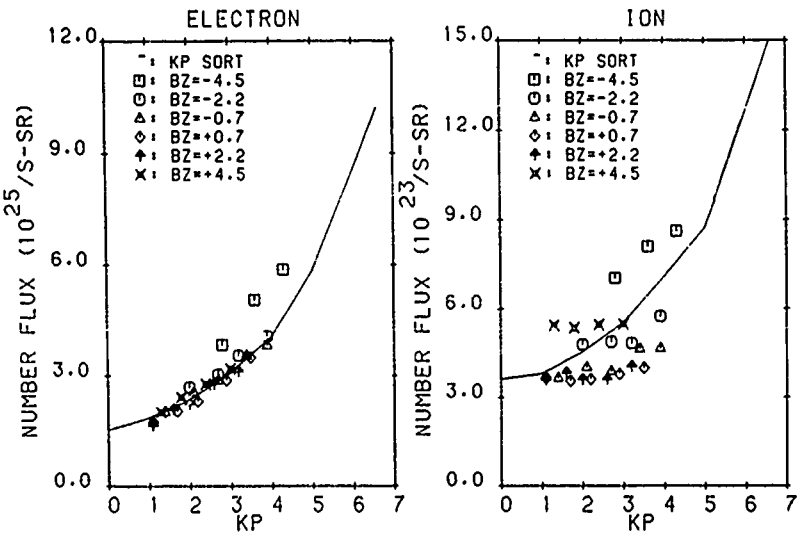

Fig. 10. Hemispheric number flux ($H_{N_{FLUX}}$) from both the Kp-ordered study and the current study, plotted as a function of Kp. (Left) Electrons. (Right) Ions.

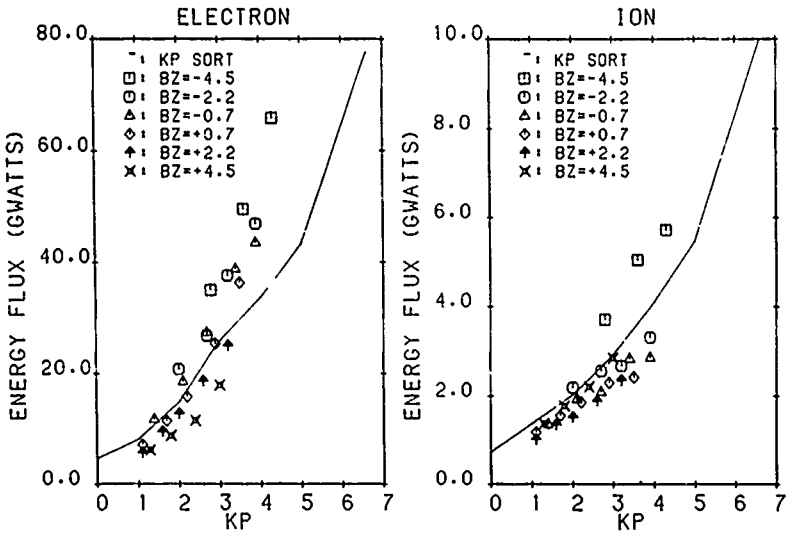

Fig. 11. Hemispheric energy flux ($H_{E_{FLUX}}$) from both the Kp-ordered study and the current study, plotted as a function of Kp. (Left) Electrons. (Right) Ions.

averaged Kp values listed in Table 2. These are shown in Figure 10 ($H_{N_{FLUX}}$ versus Kp) and Figure 11 ($H_{E_{FLUX}}$ versus Kp). In these plots the seven flux values from the earlier Kp studies have been plotted as a solid line, and the 26 flux values from the current study are marked by a symbol according to their B_z bin (independent of their V_{SW} bin). The results from the Kp statistical maps are tabulated in Table 6. Generally, there is good agreement between the two sorts. The largest discrepancies occur for the higher negative B_z cases where the values consistently tend to lie above the values for the previous Kp sort. This is most marked for the electron $H_{E_{FLUX}}$ case. This difference reflects the mixing of B_z polarities in the Kp sort as we showed for $Kp = 4$ and 6 in Figure 8. For the higher Kp level maps there is significant mixing of B_z positive with the more dominant B_z negative. Since for B_z positive the general level of precipitation is lower, to include these B_z positive periods in the Kp study decreases the average hemispheric flux as compared to the current study. The disparity in results is greatest for the electron hemispheric energy flux because the electron $H_{E_{FLUX}}$ shows the greatest response to B_z negative and thus most greatly amplifies the problem of mixing data under different B_z polarities.

Foster et al. [1986] also reported the electron hemispheric energy flux for two B_z intervals: $>+3$ nT and <-3 nT. They analyzed NOAA/TIROS satellite data and found an increase in hemispheric electron energy flux from 14 GW for their B_z positive interval to 32 GW for their B_z negative interval. For a direct comparison, we merged all our V_{SW} bins together and computed electron $H_{E_{FLUX}}$ (from unextrapolated average spectra) for the two bins with B_z intervals of +10 to +3 nT and −3 to −10 nT. We found the energy fluxes for these B_z positive and B_z negative intervals were 11 and 53 GW, respectively. Foster et al.'s wattage for B_z positive is slightly higher (×1.3) than ours, whereas their wattage for B_z negative is more significantly lower (×0.6). One source of discrepancy which could explain their lower energy input for $B_z < -3$ nT is that the NOAA/TIROS detectors have a smaller energy range, with an upper threshold of 20 keV versus our detectors' threshold of 30 keV.

7. Summary and Conclusions

Using a large data set of precipitating electron and ion measurements, we have been able to determine the variation in the hemispheric power input and number flux due to these particles as a function of polarity and magnitude of the IMF B_z component and as a function of the magnitude of the solar wind velocity. Both the hemispheric energy flux and hemispheric number flux are found to vary in a simple and consistent manner with both B_z and V_{SW}. For both electron and ion fluxes the variation with B_z (for a fixed V_{SW}) tends to a minimum for weak to moderately strong B_z positive and increases at a rate faster than linear for values both above

TABLE 6. Hemispheric Fluxes for Kp Study (Electron and Ion)

Map Number	Kp	Electron $H_{E_{FLUX}}$, GW	Electron $H_{N_{FLUX}}$, $\times 10^{25}$ (s sr)$^{-1}$	Ion $H_{E_{FLUX}}$, GW	Ion $H_{N_{FLUX}}$, $\times 10^{23}$ (s sr)$^{-1}$
1	0	4.68	1.53	0.73 (0.67)	3.62 (3.46)
2	1	8.14	1.85	1.38 (1.26)	3.80 (3.76)
3	2	14.90	2.35	2.03 (1.61)	4.54 (4.25)
4	3	25.90	3.08	2.92 (2.06)	5.53 (5.05)
5	4	33.60	4.05	4.10 (2.43)	7.10 (6.00)
6	5	43.20	5 83	5.47 (2.75)	8.74 (7.10)
7	≥6	57.60	10.20	10.00 (5.69)	15.00 (12.90)

Unextrapolated values are listed in parentheses.

and below the minimum. This effect is most marked for the ions. The variation in the fluxes with V_{sw} tends to be linear with the steepest slopes for the electron hemispheric energy flux. The variation with B_z and V_{sw} can be fit well for all four quantities by an equation either of the form

$$f(B_z, V_{sw}) = a(B_z - b)^2 + cV_{sw} + d$$

or

$$f(B_z, V_{sw}) = [a(B_z - b)^2 + 1][cV_{sw} + d].$$

Either equation indicates that no variation in B_z higher than quadratic and no variation in V_{sw} higher than linear is required. In fact, the first form shows B_z^2 and V_{sw} to be independent. This is significantly different from either the half-wave rectifier or epsilon function response.

In addition, we find that the ions make the largest contribution relative to the electrons for the lowest velocity and the highest value of B_z positive. The relative contribution decreases sharply for decreasing values of B_z positive and for increasing velocity. For B_z negative for a fixed velocity the relative contribution is approximately constant. The relative contribution of the ion to the electron number flux shows a similar variation. Also significant is that V_{sw} is most efficient in increasing energy flux during periods of B_z positive, and more so for electrons than ions.

The electron and ion total hemispheric number and energy flux represent only one product from the large data bases which have been compiled. A subsequent study utilizing the same data bases will examine the dependence of specific auroral regions on the IMF B_z and V_{sw} in terms of individual spectra and auroral boundaries. This more detailed analysis is required before one can comment further on several of the issues raised in this paper.

APPENDIX: FITTING PROCEDURE

The similarity in the variation of the four quantities with B_z and V_{sw} suggests that the variation can be fit by a relatively simple functional form. Two different approaches were taken to this fitting. In the first approach, we found that the variation with B_z in all four quantities, for a fixed V_{sw}, could be well fit by the general parabolic equation

$$f(B_z) = a_1B_z^2 + a_2B_z + a_3'.$$

Using this fact, we fit separately the B_z variation of each of the four hemispherically integrated quantities for each different velocity to an equation of this form. The resulting fit parameters a_1 and a_2, for each of the four quantities, were found to have no significant V_{sw} dependence and were thus averaged over the five velocity cases. Parameter a_3' was found to vary linearly with V_{sw} and could be fit to the linear equation

$$a_3' = a_3V_{sw} + a_4.$$

Combining these two relations gives an equation of the form

$$f(B_z, V_{sw}) = a_1B_z^2 + a_2B_z + a_3V_{sw} + a_4.$$

This equation may be expressed as

$$f(B_z, V_{sw}) = a(B_z - b)^2 + cV_{sw} + d. \quad \text{(A1)}$$

This relation shows that the data can be simply described as a family of parabolas whose minima are located at $B_z = b$ and are offset by a linear function of V_{sw}.

The second method is also based on the observation that the fluxes for each hemispheric quantity may be fit to a parabola. In this method, the fluxes as a function of B_z were normalized to the minimum flux value for a fixed V_{sw}. Since the normalized values varied only slightly with V_{sw} for a fixed B_z, the normalized values were then averaged over the different solar wind velocities and the average fit to the equation

$$f(B_z)/f(V_{sw})_{min} = a_1(B_z - a_2)^2 + a_3.$$

As in the first procedure, the variation in $f(V_{sw})_{min}$ can be approximated by the linear equation

$$f(V_{sw})_{min} = a_4V_{sw} + a_5.$$

Combining the above gives the equation

$$f(B_z, V_{sw}) = [a_1(B_z - a_2)^2 + a_3][a_4V_{sw} + a_5].$$

Factoring the a_3 out of the first bracketed expression and into the second, the equation may be simplified to

$$f(B_z, V_{sw}) = [a(B_z - b)^2 + 1][cV_{sw} + d]. \quad \text{(A2)}$$

Although the final functional forms for both methods, given as equations (A1) and (A2), have four free parameters each, the functional forms differ. Equation (A1) is the simpler, containing only the terms B_z^2, B_z, and V_{sw}. Equation (A2) contains the additional cross terms, $V_{sw}B_z$ and $V_{sw}B_z^2$. Because there are four free parameters in each method, the quality of fit should be approximately the same. Nevertheless, we can attempt to judge which method is better by investigating the goodness of fit parametrically and point by point.

The four constants, a through d, for the two methods of fitting are listed in Table 4. Two constants have the same meaning in each method and can be directly compared. The constant b equals the value of B_z that gives the minimum flux for a given V_{sw}. The constant d is the residual flux when the effects of B_z and V_{sw} are set to zero. Or alternately interpreted, $-d/c$ is the solar wind velocity that is required before there will be a positive flux into the hemisphere when $B_z = b$.

Comparing the values of b for the different types of fluxes, we find excellent overall agreement between the two methods. The worst comparison is for the case of electron energy flux where both methods show that the minimum flux is obtained for large positive B_z and the fit is done with only one half of the parabola. It is, however, interesting to note that while there is agreement between the two methods, the value of B_z for minimum flux varies greatly for the type of flux considered. It is largest for the electron $H_{N_{FLUX}}$, with an average of 3.9 ± 0.6 nT between the two methods; has an average value of 2.1 ± 0.2 nT for the electron $H_{N_{FLUX}}$ and ion $H_{E_{FLUX}}$; and is smallest for the ion $H_{N_{FLUX}}$, where both methods give ~0.95 nT. The agreement in both value and trend for the B_z that minimizes each flux does not help us to choose between the methods.

Comparing the constants d for the two methods indicates a problem whenever the values are negative, since for negative values some minimum V_{sw} must be reached before the flux will be positive when B_z is near b. Negative d values occur for the energy fluxes of both species. The minimum V_{sw} value is equal to $-d/c$. For the electron energy flux this value is 372 km/s and 211 km/s for methods 1 and 2, respectively. The former value is much too high and indicates that for low solar wind velocities method 1 will not give good values. This is the case when the values calculated from the functional form in equation (A1) are compared with data points for the lowest velocity bin. For method 2 the minimum V_{sw} for the electron energy flux is lower than measured velocities of the solar wind, and comparison of calculated and measured values shows that there is no abnormal behavior in the low-velocity bin. This same argument holds for the minimum velocities for the ion energy flux which are 95 and 80 km/s for methods 1 and 2, respectively.

Acknowledgments. The Editor thanks R. D. Zwickl and another referee for their assistance in evaluating this paper.

REFERENCES

Baker, D. N., Statistical Analyses in the study of solar wind–magnetosphere coupling, in *Solar Wind–Magnetosphere Coupling*, edited by Y. Kamide and J. A. Slavin, pp. 17–38, Terra Scientific, Tokyo, 1986.

Baker, D. N., R. D. Zwickl, S. J. Bame, E. W. Hones, Jr., B. T. Tsurutani, E. J. Smith, and S.-I. Akasofu, An ISEE 3 high time resolution study of interplanetary parameter correlations with magnetospheric activity, *J. Geophys. Res.*, *88*, 6230, 1983.

Bargatze, L. F., D. N. Baker, R. L. McPherron, and E. W. Hones, Jr., Magnetospheric response for many levels of geomagnetic activity, *J. Geophys. Res.*, *90*, 6387, 1985.

Baumjohann, W., and G. Haerendel, Magnetospheric convection observed between 0000 and 2100 LT: Solar wind and IMF dependence, *J. Geophys. Res.*, *90*, 6370, 1985.

Berthelier, A., Influence of the polarity of the interplanetary magnetic field on the annual and the diurnal variations of magnetic activity, *J. Geophys. Res.*, *81*, 4546, 1976.

Brautigam, D. H., M S. Gussenhoven, and D. A. Hardy, The IMF B_z and solar wind speed dependence for precipitating ion hemispheric energy flux, *Adv. Space Res.*, *8*, (9)65, 1988.

Burton, R. K., R. L. McPherron, and C. T. Russell, An empirical relationship between interplanetary condition and *Dst*, *J. Geophys. Res.*, *80*, 4204, 1975.

Couzens, D. A., and J. A. King, Interplanetary medium data book, supplement 3, 1977–1985, *Rep. NSSDC 86-04*, Natl. Space Sci. Data Center, World Data Center A for Rockets and Satellites, Greenbelt, Md., April 1986.

Couzens, D. A., and J. A. King, Interplanetary medium data book, supplement 4, 1985–1988, *Rep. NSSDC 89-17*, Natl. Space Sci. Data Center, World Data Center A for Rockets and Satellites, Greenbelt, Md., Sept. 1989.

Foster, J. C., J. M. Holt, R. G. Musgrove, and D. S. Evans, Solar wind dependencies of high-latitude convection and precipitation. in *Solar Wind–Magnetosphere Coupling*, edited by Y. Kamide and J. A. Slavin, pp. 477–494, Terra Scientific, Tokyo, 1986.

Gussenhoven, M. S., Extremely high latitude auroras, *J. Geophys. Res.*, *87*, 2401, 1982.

Gussenhoven, M. S., Low-altitude convection, precipitation, and current patterns in the baseline magnetosphere, *Revi. Geophys.*, *26*, 792, 1988.

Hardy, D. A., W. J. Burke, M. S. Gussenhoven, N. Heinemann, and E. Holeman, DMSP/F2 electron observations of equatorward auroral boundaries and their relationship to the solar wind velocity and the north-south component of the interplanetary magnetic field, *J. Geophys. Res.*, *86*, 9961, 1981.

Hardy, D. A., W. J. Burke, and M. S. Gussenhoven, DMSP optical and electron measurements in the vicinity of polar cap arcs, *J. Geophys. Res.*, *87*, 2413, 1982.

Hardy, D. A., L. K. Schmitt, M. S. Gussenhoven, F. J. Marshall, H. C. Yeh, T. L. Schumaker, A. Huber, and J. Pantazis, Precipitating electron and ion detectors (SSJ/4) for the block 5D/flight 6-10 DMSP satellites: Calibration and data presentation, *Rep. AFGL-TR-84-0314*, Air Force Geophys. Lab., Hanscom Air Force Base, Bedford, Mass., 1984.

Hardy, D. A., M. S. Gussenhoven, and E. Holeman, A statistical model of auroral electron precipitation, *J. Geophys. Res.*, *90*, 4429, 1985.

Hardy, D. A., M. S. Gussenhoven, and D. H. Brautigam, A statistical model of auroral ion precipitation, *J. Geophys. Res.*, *94*, 370, 1989.

Iijima, T., and T. Shibaji, Global characteristics of northward IMF-associated (NBZ) field-aligned currents, *J. Geophys. Res.*, *92*, 2408, 1987.

Maezawa, K., Statistical study of the dependence of geomagnetic activity on solar wind parameters, in *Quantitative Modeling of Magnetospheric Processes*, *Geophys. Monogr. Ser.*, vol. 21, edited by W. P. Olson, pp. 436–447, AGU, Washington, D. C., 1979.

Maezawa, K., and T. Murayama, Solar wind velocity effects on the auroral zone magnetic disturbances, in *Solar Wind–Magnetosphere Coupling*, edited by Y. Kamide and J. A. Slavin, pp. 59–84, Terra Scientific, Tokyo, 1986.

Makita, K., C.-I. Meng, and S.-I. Akasofu, The shift of the auroral electron precipitation boundaries in the dawn-dusk sector in association with geomagnetic activity and interplanetary magnetic field, *J. Geophys. Res.*, *88*, 7967, 1983.

Makita, K., C.-I. Meng, and S.-I. Akasofu, Latitudinal electron precipitation patterns during large and small IMF magnitudes for northward IMF conditions, *J. Geophys. Res.*, *93*, 97, 1988.

Murayama, T., Coupling function between solar wind parameters and geomagnetic indices, *Rev. Geophys.*, *20*, 623, 1982.

Nakai, H., and Y. Kamide, Response of nightside auroral oval boundaries to the interplanetary magnetic field, *J. Geophys. Res.*, *88*, 4005, 1983.

Reiff, P. H., and J. G. Luhmann, Solar wind control of the polar-cap voltage, in *Solar Wind–Magnetosphere Coupling*, edited by Y. Kamide and J. A. Slavin, pp. 453–476, Terra Scientific, Tokyo, 1986.

Rich, F. J., D. A. Hardy, R. H. Redus, and M. S. Gussenhoven, Northward IMF and patterns of high-latitude precipitation and field-aligned currents: The February 1986 storm, *J. Geophys. Res.*, *95*, 7893, 1990.

Rossberg, L., A close look at the solar wind–magnetosphere interaction, *J. Geophys. Res.*, *89*, 2162, 1984.

Rossberg, L., The effect of the solar wind velocity on substorm activity, *J. Geophys. Res.*, *94*, 13,571, 1989.

Russell, C. T., Solar wind control of magnetospheric configuration, in *Solar Wind–Magnetosphere Coupling*, edited by Y. Kamide and J. A. Slavin, p. 209, Terra Scientific, Tokyo, 1986.

Scurry, L., and C. T. Russell, Geomagnetic activity for northward B_z (abstract), *Eos Trans. AGU*, *70*, 1280, 1989.

Spiro, R. W., P. H. Reiff, and L. J. Maher, Jr., Precipitating electron energy flux and auroral zone conductances: An empirical model, *J. Geophys. Res.*, *86*, 8215, 1982.

Spreiter, J. R., and A. Y. Alksne, Plasma flow around the magnetosphere, *Rev. Geophys.*, *7*, 11, 1969.

Wallis, D. D., and E. E. Budzinski, Empirical models of height-integrated conductivities, *J. Geophys. Res.*, *86*, 125, 1981.

Zanetti, L. J., and T. A. Potemra, The relationship of Birkeland and ionospheric current systems to the interplanetary field, in *Solar Wind–Magnetosphere Coupling*, edited by Y. Kamide and J. A. Slavin, pp. 547–562, Terra Scientific, Tokyo, 1986.

D. H. Brautigam, M. S. Gussenhoven, and D. A. Hardy, Geophysics Laboratory, Hanscom Air Force Base, MA 01731.

(Received June 22, 1990;
revised October 23, 1990;
accepted January 10, 1991.)